





Structure formation by electrostatic interactions in strongly coupled medium

Mamta Yadav ^{1,*}, Priya Deshwal ¹, Srimanta Maity ², and Amita Das ^{1,†}

¹*Department of Physics, Indian Institute of Technology Delhi, Hauz Khas, New Delhi 110016, India*

²*ELI Beamlines Facility, The Extreme Light Infrastructure ERIC, Za Radnicí 835, 25241 Dolní Břežany, Czech Republic*



(Received 4 January 2023; revised 13 March 2023; accepted 8 May 2023; published 24 May 2023)

The formation of correlated structures is of importance in many diverse contexts such as strongly coupled plasmas, soft matter, and even biological mediums. In all these contexts the dynamics are mainly governed by electrostatic interactions and result in the formation of a variety of structures. In this study, the process of formation of structures is investigated with the help of molecular dynamics (MD) simulations in two and three dimensions. The overall medium has been modeled with an equal number of positive and negatively charged particles interacting via long-range pair Coulomb potential. A repulsive short-range Lennard-Jones (LJ) potential is added to take care of the blowing up of attractive Coulomb interaction between unlike charges. In the strongly coupled regime, a variety of classical bound states form. However, complete crystallization of the system, as typically observed in the context of one-component strongly coupled plasmas, does not occur. The influence of localized perturbation in the system has also been studied. The formation of a crystalline pattern of shielding clouds around this disturbance is observed. The spatial properties of the shielding structure have been analyzed using the radial distribution function and Voronoi diagram. The process of accumulation of oppositely charged particles around the disturbance triggers a lot of dynamic activity in the bulk of the medium. As a result of this, close encounters are possible even between those particles/clusters which were initially and/or at some point of time widely separated. This leads to the formation of a larger number of bigger clusters. There are, however, also instances when bound pairs break up and the electrons from bound pairs contribute to the shielding cloud, whereas ions bounce back into the bulk. A detailed discussion of these features has been provided in the manuscript.

DOI: [10.1103/PhysRevE.107.055214](https://doi.org/10.1103/PhysRevE.107.055214)

I. INTRODUCTION

Electrostatic interactions play an overwhelmingly important role and form the basis of many processes, involving plasmas [1–3], soft matter [4], biological medium [5,6], etc. In these cases, the system is often modeled by variants of Langevin and Fokker Planck equations involving electrostatic interactions (e.g., the Poisson-Nernst-Planck equations [7,8]). Formations of colloidal suspensions, polymers, and clusters in these contexts have always attracted attention and often have significant technological and scientific relevance. Our attempt here is to understand the process of structure formation with the help of molecular dynamics (MD) simulations in the simplest scenario of a collection of uniformly distributed charged particles of both signs, interacting via long-range Coulomb force along with Lennard-Jones (LJ) interaction. The LJ potential helps in switching off the attractive Coulomb interaction amidst oppositely charged particles at short distances preventing their collapse. One is thus seeking the formation of clusters in this medium, wherein two or more particles join together to form a stable bound configuration. It is clear that the thermal effects will let the particles fly away inhibiting the survival of any such binding configuration. However, if the

medium is in a strongly coupled state for which the mutual interaction energy exceeds the thermal energy, the possibility of the formation of such a bound state exists. We, therefore, explore the dynamics in the strongly coupled regime for this medium.

We have chosen a collection of equal and oppositely charged particles interacting with electrostatic Coulomb and LJ potential in the strongly coupled regime for our model. This is essentially like a quasineutral strongly coupled plasma state of matter [9,10]. Preparation of a strongly coupled plasma medium is usually a challenge as it is typically created by doing violence to matter and hence is seething with thermal energy. The strongly coupled state requires that the parameter $\Gamma = Q^2/aK_bT > 1$, where Q is the charge state of the particle, a is the inter-particle separation and T is the temperature and K_b is the Boltzmann constant. Thus, the strong coupling condition can be achieved by (i) enhancing the charge Q , (ii) reducing the inter-particle distance a , and (iii) decreasing the temperature T .

Working with high Q particles has led to the observation of strong coupling effects even at room temperatures in dusty plasmas [11,12] in the form of crystallization of highly charged micron-sized dust particles against a background of normal electron-ion plasma. The strongly coupled dusty plasma medium has garnered a lot of attention in the plasma community for a couple of decades now. The strong coupling effects playing a distinct role in the collective modes

*ymamta358@gmail.com

†amita@iitd.ac.in, amitadas3@yahoo.com

have been studied extensively both theoretically [13] and experimentally [14]. For the strongly coupled dusty plasma medium properties like collective structures [15–17], linear and nonlinear waves [18–20], instabilities [21–24], and phase transitions [25,26] have been observed. The interplay of single particle and collective dusty plasma dynamics has also been studied [27]. The dynamics of small dust clusters have illustrated dynamical equilibrium states with chaotic motion [28,29].

In superdense stars [30], the interior of planets, inertial confinement plasmas, etc., the reduction of interparticle separation a can lead to strong coupling behavior. In some of these contexts, however, the dynamics might involve electromagnetic effects. There has also been tremendous progress in the creation of ultracold plasma experimentally using laser-cooling techniques. For instance, xenon atoms via a photo-ionization process are confined by a magneto-optical trap [31–33] with typical density in the range of 10^5 cm^{-3} to 10^{10} cm^{-3} with either both or one of the species in a strongly coupled state. Many properties of ultracold plasma have been studied like the formation of Rydberg atoms [33]. Any heating in such a system needs to be avoided to keep the system in a strongly coupled state. For this, studies have been conducted to identify and restrict the inherent heating mechanisms that are prevalent in these systems. Mechanisms such as disorder-induced heating [34,35] and three-body recombination (3BR) [36] have been identified as some prominent factors causing the heating of the medium. A study of thermodynamics and transport properties such as pressure and internal energy [37], etc., has also attracted attention. It is also interesting to note that studies in magnetically confined plasma [38] have shown ions in the strong coupling regime arranged in concentric shells and demonstrate solid and liquidlike behavior. In another work by Pohl *et al.* [39] the crystallized structure was observed at the center of expanding laser-cooled ultracold plasma in which short-range concentric ion shells are formed with appropriate initial conditions.

Our objective here is to explore the possibility and nature of structure formation in a neutral plasma. The study also has relevance in other contexts of soft matter, and biological systems in which structure formation is an important issue, and electrostatic interactions are believed to be responsible for the same. Here, one is seeking the formation of structures with the most elementary coulomb interaction with Lennard Jones potential at short distances to avoid the collapse of unlike charged particles. We make use of the open-source molecular dynamics code of LAMMPS for carrying out these studies numerically.

This article has been organized as follows. In Sec. II, we discuss the simulation setup and the choice of parameters. In Sec. III, we investigate the formation of classical bound states. In Secs. IV and V, we study the effect of an external perturbation introduced in the two-dimensional (2D) and three-dimensional (3D) simulation systems. The perturbation is in the form of inserting a massive and heavily charged particle into the medium. This could be equivalent to applying a biased probe in experiments. This inserted particle remains fixed in space while the particles in the medium respond to its potential. The charge in it is chosen to be quite high, about two orders higher than the charge of other

particles in the system. The evolution of the system is studied in both two and three dimensions. Oppositely charged particles assemble around the externally placed charge particle to screen its potential. However, when the underlying plasma is strongly coupled, the oppositely charged particles assemble in a crystalline pattern around it. The behavior of the crystalline pattern is understood with the help of the radial distribution function and Voronoi diagrams. As expected the potential due to this crystalline charge cloud typically resembles the Debye shielding profile. However, there are some deviations, arising due to the crystalline and discrete nature of the shielding cloud. The value of σ , which typically defines the distance where the LJ repulsive potential goes to zero, is also found to play a role. The role of external perturbation on the formation and existence of the seemingly fragile classical bound state is studied. It is observed that the disturbance induced by the insertion of the external highly charged particle leads to the formation of higher numbers of bigger-sized bound state clusters. This happens as the particles placed far apart now get an opportunity for close encounters. However, in all these simulations no three-dimensional bound state structure formation was observed. In Sec. VI it is shown that when some bound states are evolved in isolation (absence of other plasma particles) they reorganize as three-dimensional bound structures. In fact, it is shown that the 3D structures that form are energetically favorable. Yet such structures do not form in the backdrop of plasma medium. It clearly shows that the plasma medium plays an important role in the formation of the clusters. In Sec. VII we summarize and conclude our studies.

II. MD SIMULATION DETAILS

We have carried out 2D and 3D molecular dynamics simulations using an open-source classical MD simulation software LAMMPS [40]. We have typically used the parameters associated with electron-ion plasma in an ultracold regime. The particles in the simulation box is interacting with each other through the long-range pair Coulomb potential (V_{PC}) and an additional short-range repulsive LJ potential (V_{LJ}) as given by

$$V(r_{kl}) = V_{\text{PC}} + V_{\text{LJ}}, \quad (1)$$

where

$$V_{\text{PC}} = \frac{Q_l}{4\pi\epsilon_0 r_{kl}}, \quad (2)$$

$$V_{\text{LJ}} = 4\epsilon \left[\left(\frac{\sigma}{r_{kl}} \right)^{12} - \left(\frac{\sigma}{r_{kl}} \right)^6 \right]. \quad (3)$$

This short-range LJ potential avoids the recombination of electrons and ions. Here Q_l define the charge on any l th particle. Also, r_{kl} represents the distance between k th and l th particles. Here, ϵ and σ are the usual Lennard-Jones potential parameters where ϵ defines the strength of the LJ potential well and σ describes the distance at which interparticle LJ potential becomes zero. The PPPM (particle-particle particle-mesh) method [41] is used for the calculation of long-range Coulomb interactions. In our case, we have assumed both electrons and ions to be in a strongly coupled regime which

means the coulomb coupling parameter (Γ) for both species is greater than unity. The equation of motion of any k th particle can be expressed as

$$m_k \frac{d^2 \mathbf{r}_k}{dt^2} = -Q_k \nabla \sum_{l=1}^{N-1} V_{\text{pC}} - \nabla \sum_{l=1}^{N-1} V_{\text{LJ}}, \quad (4)$$

where N is the total number of particles in the system.

In the two-dimensional (2D) study, we have chosen a rectangular simulation box of length $L_x = L_y = 1.4 \times 10^{-3}$ m in the \hat{x} and \hat{y} directions, respectively. Periodic boundary conditions are considered in all directions. Initially, 10^4 electrons and 10^4 ions with densities 1.0×10^{10} m $^{-2}$ are distributed randomly inside the simulation box. This ensures that there exist no initial spatial pre-correlations between the charged particles. The charge (Q_i) and mass (m_i) of the ion are taken to be 1.6×10^{-19} C and $100m_e$, respectively. Here, m_e is the mass of an electron, i.e., $m_e = 9.109 \times 10^{-31}$ Kg. The mass of the ion in simulation is chosen smaller compared to even the proton mass, merely to reduce the simulation time. In our simulations, the temperature of electrons and ions are both considered to be equal and at $T_e = T_i = 0.1$ K. All the length scales are normalized by the average interparticle distance a . In 2D, the average interparticle distance a and the areal density n are related as $a = (n\pi)^{-1/2}$. Thus, for our choice of n , the value of average interparticle distance turns out to be $a = 5.64 \times 10^{-6}$ m. In our simulations, the time scales are normalized by ω_{pe}^{-1} , where $\omega_{\text{pe}} = (ne^2/m_e\epsilon_0)^{1/2}$ is electron-plasma frequency. The dynamics of the lightest species (i.e., electrons) are tracked by choosing the time step $3 \times 10^{-8} \omega_{\text{pe}}^{-1}$.

In our 3D simulations, we have taken the length of the simulation box to be $L_x = L_y = L_z = 3.7 \times 10^{-5}$ m, in \hat{x} , \hat{y} , and \hat{z} directions, respectively. We have chosen the periodic boundary conditions in all directions. Again, 10^4 electrons and 10^4 ions with densities 3.7×10^{17} m $^{-3}$ are initially distributed randomly inside the simulation box. The relation between density n and average interparticle distance is $a = [3/(4n\pi)]^{1/3}$. The temperature of electrons and ions is chosen to be $T_e = T_i = 1$ K, which corresponds to the Coulomb coupling parameter $\Gamma = 20$, i.e., in the strongly coupled regime. The time step is chosen as $3 \times 10^{-5} \omega_{\text{pe}}^{-1}$ for this case. This is also small enough to track the dynamics of the lightest electron species.

As mentioned earlier, particles (both electrons and ions) are interacting with long-range pair Coulomb potential. Additionally, a short-range LJ pair potential is present in the pair interactions between particles. The parameters associated with these interaction potentials are as follows. The cutoff distance for Coulomb pair potential is chosen to be $r_c = 20a$. The parameter σ associated with the LJ potential is chosen to be $10^{-2}a$ for most of the simulation studies. We have, however, also varied the value of σ . The normalized parameter ϵ is chosen to be $558K_B T$ and $75K_B T$ for 2D and 3D, respectively. In both 2D and 3D simulations, Nose-Hoover thermostats [42,43] have been used to achieve the thermal equilibrium associated with the desired value of Coulomb coupling parameter Γ .

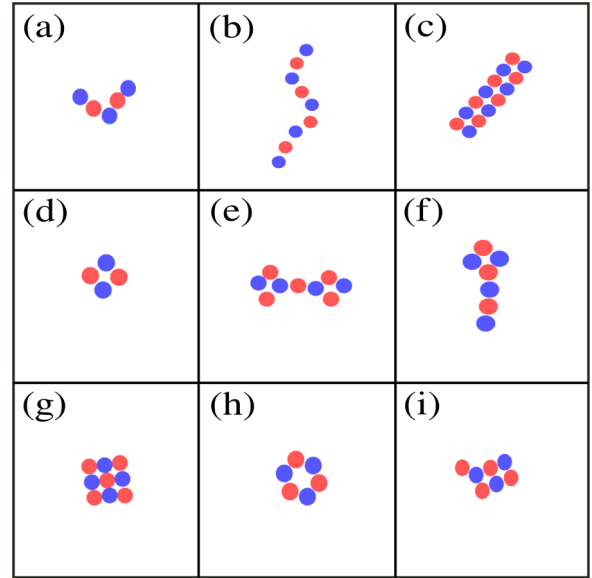


FIG. 1. Distinct variety of bound structures at equilibrium. Here, the red and blue dots correspond to the electrons and ions, respectively. This is for the case where $m_i = 100 m_e$.

III. FORMATION OF BOUND STRUCTURES FOR THE SYSTEM IN EQUILIBRIUM

Once the system achieves thermodynamic equilibrium with the attached thermostat, its evolution shows the formation of several distinct varieties of bound structures. In these structures, a few electrons and ions combine with each other and form a stable configuration. Some such structures have been displayed in Fig. 1. There are linear structures as shown in Figs. 1(a) and 1(b). In fact, in Fig. 1(b) about nine particles (four electrons and five ions) have joined together to form a linear chain. Such linear chains have alternating particles with opposite signs attached together. Figure 1(c) shows a 2D structure in which two linear chains join adjacently to form a 2D structure. In Fig. 1(d) we have shown the formation of a square structure in which the diagonally opposite particles are of the same sign. Two such square structures can join together as shown in Fig. 1(e) or a square can have a linear chain attached to itself as shown in Fig. 1(f) resembling a kite. Figure 1(g) is again a square structure with nine particles, each side of the square having three particles. The circular ringed structure in Fig. 1(h) forms when the particles at the end of the linear chain join together. Figure 1(i) is again a kite-like structure like that shown in Fig. 1(f). It should be noted that the bound structures that form do not necessarily have an equal number of ions and electrons. A mismatch of one unit charge (but not higher than this) has been observed.

The structures shown in Fig. 1 are not unique in terms of the number of particles forming that particular shape. Linear chains with a larger number of particles are also observed to get formed. The kite-like structure shown in Fig. 1(f) may have a longer linear chain attached to it. It is also interesting to note that with the same number of particles different kinds of structures have been observed to form. For instance, the structures shown in Figs. 1(b), 1(e), and 1(g) all have nine particles. However, the form of these structures is quite

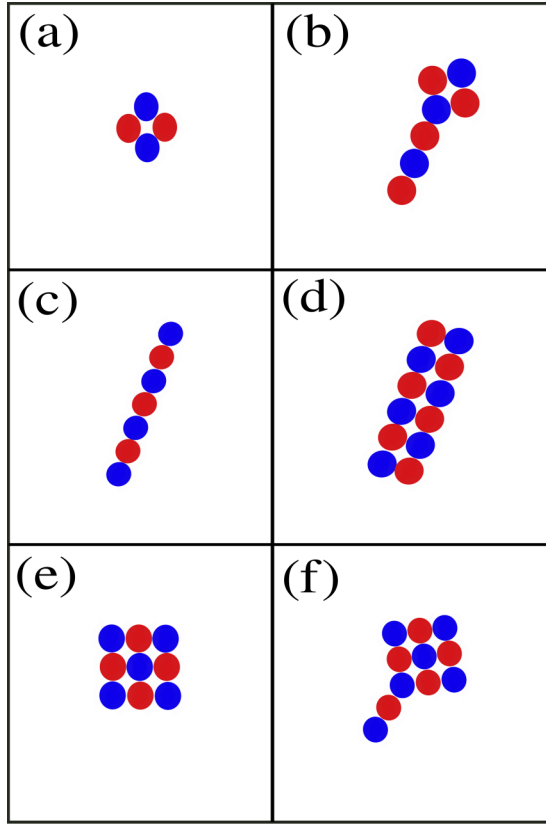


FIG. 2. Formation of bound structures at equilibrium when $m_i = 1836 m_e$. Here, the red and blue dots correspond to the electrons and ions, respectively.

different. In fact, some other kinds of structures can also form with nine particles. These structures form during various stages of evolution and seem to have small differences in their bound state energy. We have captured one such transition event taking place during the evolution where the linear structure of seven particles first joins with two particles to form a nine-particle linear structure. This nine-particle linear structure eventually forms a kitelike structure. This subsequently transforms to the square lattice structure of subplot(g). This can be observed from a video “Transition.mp4” [44] attached as Supplemental Material. The potential energies corresponding to the nine particle configurations in Figs. 1(b), 1(e), and 1(g) have been obtained in Appendix. They have the values of -0.47×10^{-21} J, -2.29×10^{-21} J, and -4.13×10^{-21} J, respectively, for the chosen parameters of our simulation. The binding energy of the square lattice being the highest is observed to form ultimately in the movie also.

We also carried out 2D simulations with the realistic ion mass $m_i = 1836 m_e$. Even for this case, the evolution shows the formation of a distinct variety of bound structures as shown in Fig. 2. For this case, we observe the same phenomena as in the earlier case, but we have to evolve simulations for a longer time to observe the behavior. To save the computational cost we have considered $m_i = 100 m_e$ in most of our simulations.

We illustrate the dynamical process of formation of some of these structures in Fig. 3 by showing the snapshot of a

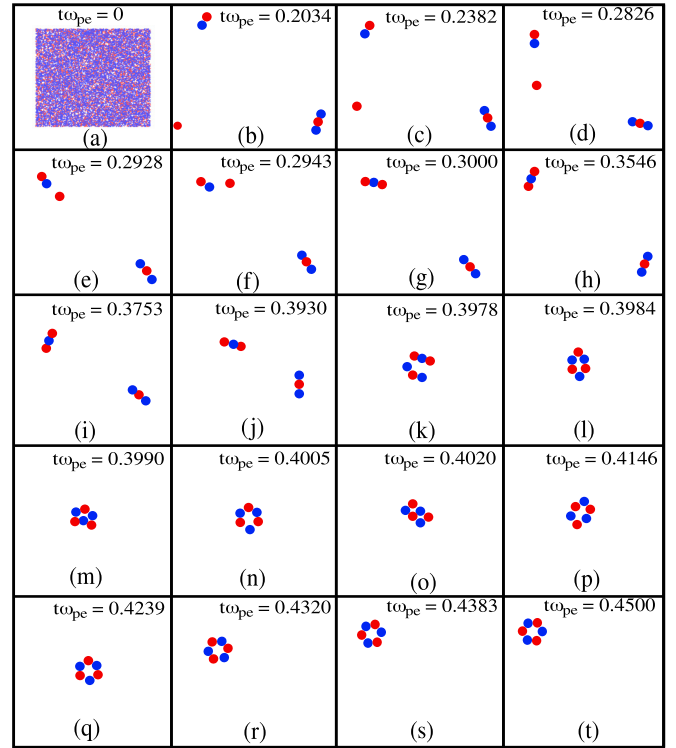


FIG. 3. The schematics for the time evolution of one kind of bound structure. Blue dots and red dots represent the ions and electrons, respectively. The normalized time is varying from $t\omega_{pe}$ 0.2034 to 0.45 and $t\omega_{pe} = 0$ represents the distribution of electrons and ions initially in the simulation box.

particular zoomed region from the entire simulation region which has been shown in Fig. 3(a) of the figure at $t\omega_{pe} = 0$, where the randomly distributed particles have been shown. From Figs. 3(b) to 3(t) we show the snapshots at various times for a zoomed region from the simulation box containing six particles. The entire dynamics is covered within a fraction of the plasma period. During this period no other particle entered this region hence the particle number remained at six. From Fig. 3(b) to 3(f) one can observe the attachment of an electron to an ion-electron pair placed at the top of the box. A three-particle linear chain can be observed to be rotating at the bottom right corner of the subplot. From Fig. 3(g) to 3(k) one can observe how the two three-particle linear chains approach each other and join together. After combining, they wiggle a lot going through a variety of phases shown in Fig. 3(l) to 3(p). Finally, as they relax they form a ringed structure which is found to be stable. A movie “Bound.mp4” [44] has been prepared as Supplemental Material from $t\omega_{pe}$ 0.2034 to 0.45 to show the formation of bound structure in more detail.

We would like to emphasize here that, while the simulations have been carried out both in 2D and 3D, we observe no formation of three-dimensional clusters. In the next section, we observe what happens to these structures when the medium is perturbed by inserting a highly charged heavy particle having no dynamics of its own. We also study how the plasma particles accumulate around the external perturbation to shield its potential.

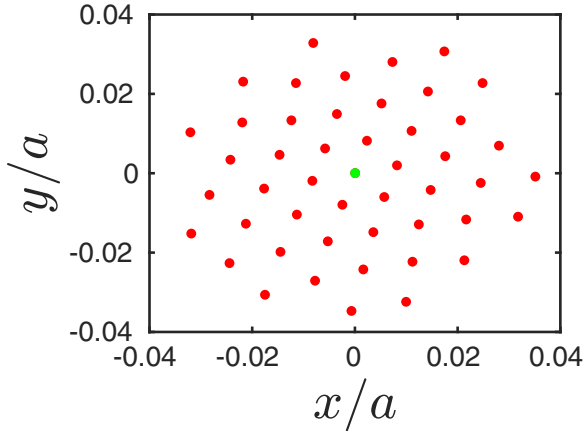


FIG. 4. Arrangements of electrons around external perturbation. The green dot represents the external perturbation that is introduced at the center of the simulation box and the red dots represents electrons.

IV. STRUCTURE FORMATION IN A TWO-DIMENSIONAL PERTURBED SYSTEM

When a weakly coupled plasma is disturbed by an external potential, the plasma tries to shield this potential within a distance of Debye length. It is, however, not clear how a strongly coupled plasma would react to an externally applied field. In this section, we try to explore this particular issue in a two-dimensional simulation set-up. Once the system gets settled in thermal equilibrium an external point charge is inserted at the center of the simulation box. The mass (M_P) and charge (Q_P) of external perturbation are chosen to be large as $100m_i$ and $100Q_i$, respectively. Since the externally inserted charge has a very high mass it remains stationary and is not allowed to move. The electrons get attracted towards this externally applied positive charge whilst the ions are repelled from it. The insertion thus initiates a dynamical response from the plasma. We investigate the behavior of the shielding cloud that accumulates around this charge and also the influence of such a dynamic response from the plasma on the classical bound pairs. It is observed that the shielding occurs in the form of an electron cloud arranged in a crystalline pattern due to the strongly coupled nature. It is interesting to note that despite the plasma getting perturbed, even bigger-sized bound state clusters form in the bulk region. We discuss these two effects in the subsequent subsections.

A. The structure of shielding cloud

Figure 4 represents the arrangements of electrons around the external perturbation at a time ($t\omega_{pe} = 15.93$) after the charge has been inserted. The central green dot represents the externally inserted high positively charged perturbation, and the red dots correspond to the electrons that accumulate around it. The process of accumulation is slow as electrons came one by one from bulk plasma and get arranged in a hexagonal lattice structure of Fig. 4. After completing the first shell electrons start arranging in the next shell and so on. The addition of a single highly charged point particle attracts particles of opposite sign near itself while repelling those of

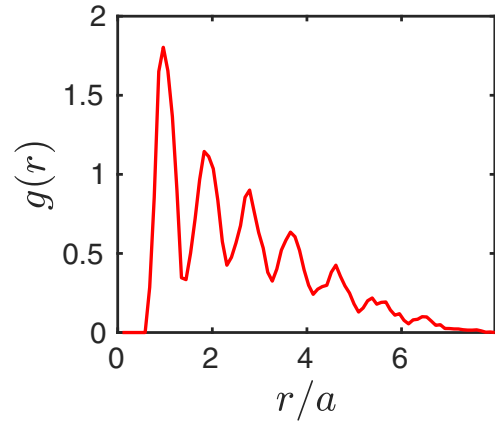


FIG. 5. Radial distribution function as a function of distance from external perturbation at time ($t\omega_{pe}$) 15.93.

like sign. This accumulation of oppositely signed particles now constitutes a one-component plasma/cluster of particles acted upon by a strong radial confining force. It is well known that a one-component plasma in 2D forms a hexagonal lattice structure. The presence of radial confining force and a finite extent/number of particles cause distortions to the hexagonal structure as is evident from the figures. We have shown the radial distribution function (RDF), measuring the probability distribution of finding the electrons with the inserted external particle as the reference in Fig. 5. The various peaks in the structure corresponds to the various rings/shells that are present in the crystalline structure formed by the electrons around the reference particle that has been introduced. Figure 6 represents the Voronoi diagram for the shielding cloud which is shown in Fig. 4. This provides information about the nearest neighbor of each particle in the cluster by constructing polygons around each point. The boundary of the polygon is constructed by bifurcating the distance between the particle and its nearest neighbours. We illustrate the formation of hexagons and pentagons with yellow and cyan colors, respectively. It is clear from the Voronoi diagram that the

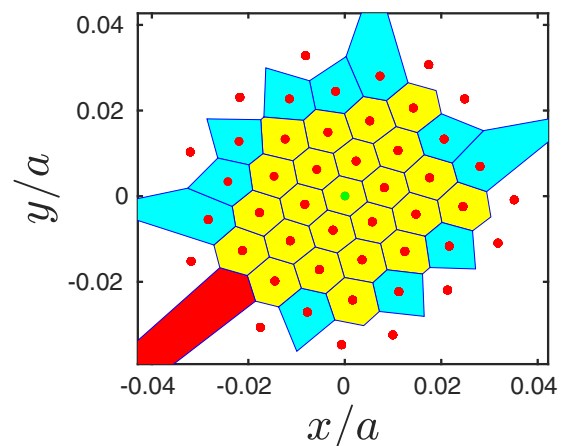


FIG. 6. Voronoi diagram of electrons around external perturbation. Voronoi cells in yellow color represent the six nearest neighbors, whereas cyan color denotes five neighbors.

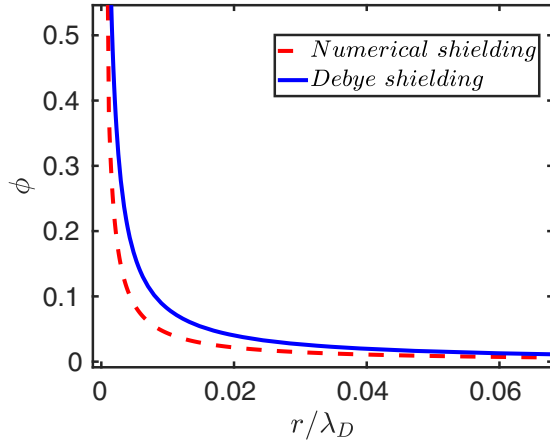


FIG. 7. Plot of potential profile as a function of normalized distance from external perturbation having charge $100Q_i$. Here, the blue and red curve corresponds to potential in normal electron-ion plasma and ultracold plasma, respectively.

shielding cloud arranges itself in the hexagonal lattice. The pentagonal structure arises at the boundary of the cloud.

Once the shielding process gets completed and the plasma becomes quiescent, we decide to study the potential profile of the shielding cloud to determine whether it resembles the Debye shielding form encountered in the weakly coupled regime. The value of Debye length as estimated from the choice of our simulation parameters is $\lambda_D = 1.7 \times 10^{-4}$ m. The theoretical Debye shielding profile using this particular value of λ_D along with the one obtained from the simulation has been shown in Fig. 7 by solid blue and red dashed lines, respectively. The plot clearly shows that while there is an agreement in both the plots at higher values of r/λ_D , at shorter distances the simulation depicts a sharper screening. Here, the value of $\sigma = 5.64 \times 10^{-8}$ m is chosen to be shorter than the Debye length. In fact we observe that the value of σ plays a crucial role in defining the screening now. In the next section, this is discussed in the context of 3D simulations.

B. Impact on bound structures in bulk

We now study the effect this perturbation has on the formation of bound structures in the bulk. The perturbed system initiates a dynamical response by the plasma. While the electrons get preferentially attracted to shield the charge of the particle introduced in the medium, they even drag along with them some of the bound structures to which they are attached. In Fig. 8, we show through snapshots of various times, how free electrons get attracted towards the disturbance one by one and get attached to it forming a lattice structure around it. It can be observed from Figs. 8(e) to 8(l) that even bound states get dragged by the electrons toward the structure. Upon reaching a very close distance the bound cluster gets dissociated and leaves the electron in it to contribute to the screening cloud, while the ion rebounds back to the bulk. To understand this evolution of structure more clearly the movie “Evolution.mp4” [44] has been prepared as Supplemental Material. However, despite such disassociation of the bound structures, it is interesting to note that the

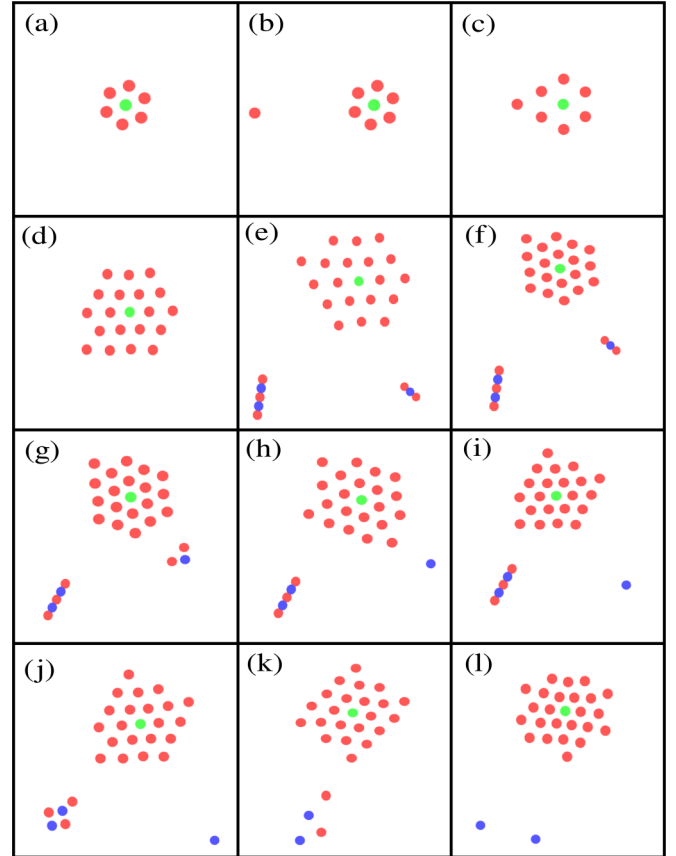


FIG. 8. Evolution of structure around the external perturbation. Here, red, blue, and green dots correspond to electrons, ions, and externally introduced perturbation, respectively.

increased activity allows for more encounters amidst particles in the bulk resulting in larger and more complex shaped structure formation as has been depicted in Fig. 9. These bigger structures were not observed in simulations when no external perturbation was introduced. In fact, in Fig. 8 itself, it can be observed that a linear chain hovering around the structure at the left-down corner gets converted into a complex kitelike pattern in Fig. 8(j). However, subsequently, it too being very close to perturbation donates all its electrons to the shielding cloud and the two ions bounce back.

V. EXTERNAL PERTURBATION IN 3D SYSTEM

We have also carried out our simulation studies in three dimensions. We distribute 10^4 electrons and 10^4 ions randomly in the simulation box and seek the attainment of thermodynamic equilibrium at the desired temperature. Thereafter, we perturb the system by inserting a massive particle having a charge of $100Q_i$ at the center of the simulation box. Since the inserted particle has a positive charge again the electrons in the system rush to shield its charge. This time, however, the system is three-dimensional so the electrons form a three-dimensional shielding cloud. We now investigate whether the shielding cloud has a crystalline form and if so what kind of arrangement takes place in the cloud. As the structure cannot be visualized in 3D we have employed certain diagnostics to perceive it in the best possible manner.

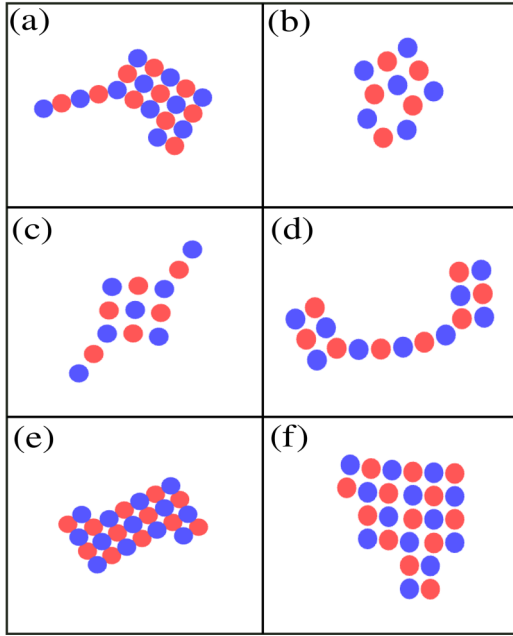


FIG. 9. More complex bound structures formed in bulk of plasma when the external perturbation is introduced.

A. Form of the shielding cloud

In Figs. 10(a) and 10(b) the projection of all electrons in the x - y and x - z planes have been shown. The central point represented by the green star is the reference point for the highly charged particle introduced as an external perturbation in the system. In both subplots, almost all positions are enclosed within the dotted circles which signifies that the cluster structure has isotropic spherical confinement. The arrangement appears to be random and isotropic from this perspective. However, the shell structure of the arrangement is pretty evident when we choose to plot the locations of the electrons involved in shielding in terms of cylindrical coordinates $\rho = \sqrt{(x^2 + y^2)}$ and z in Fig. 11. As z could be any axis so it is evident that the arrangement is in the form of spherical shells around the external perturbation introduced in the medium. The radial distribution function plotted in Fig. 12 having peaks confirms further the formation of the shell structure. The Voronoi diagram in the 3D spherical shell

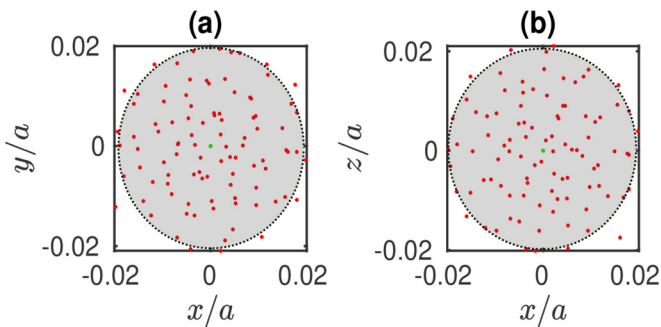


FIG. 10. The projection of all the electrons that are involved in structure formation around external perturbation (green star) in (a) horizontal plane ($x - y$ plane) and (b) vertical plane ($x - z$ plane).

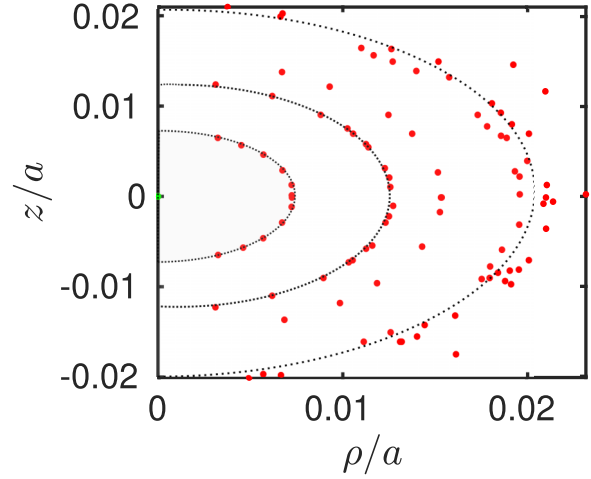


FIG. 11. Shell structure by the projection of all the electrons into the ρ - z plane. Most occupied Shells are represented by the black dotted lines and the green dot corresponds to external perturbation.

has been shown in Fig. 13 at the radius of the various rings determined from the plot of Fig. 11. The coordinate axes depicted in Fig. 13 is normalized by the radius of that particular shell. The number of polygons appearing in various shells has been counted and shown in Table I. The pentagons appear to be the dominant form in the first two shells. However, the third shell shows hexagons to be dominant. With different choices of charges taken for the inserted particles, we observe the same spherical arrangement of electrons. The innermost shell has 12 electrons and the second and the last shell have 20 and 50 electrons, respectively.

B. Time evolution of structure in 3D

We also investigate how the shielding process progresses in time. For this purpose, we track the number of electrons as they collect around the externally introduced particle. In

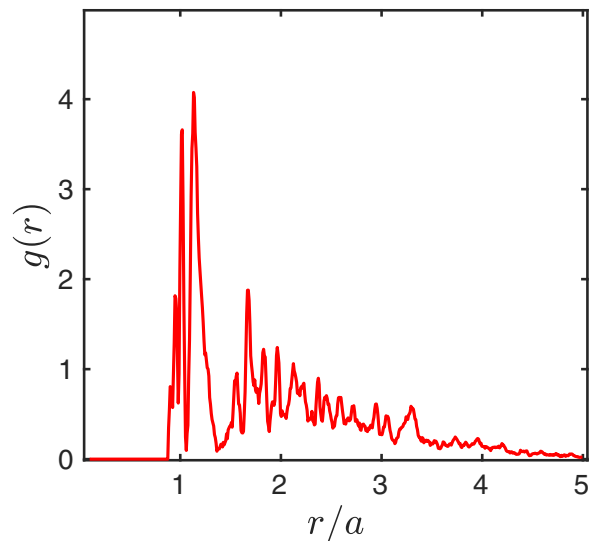


FIG. 12. Radial distribution function as a function of distance from the externally introduced perturbation at the time ($t\omega_{pe}$) 218.7.

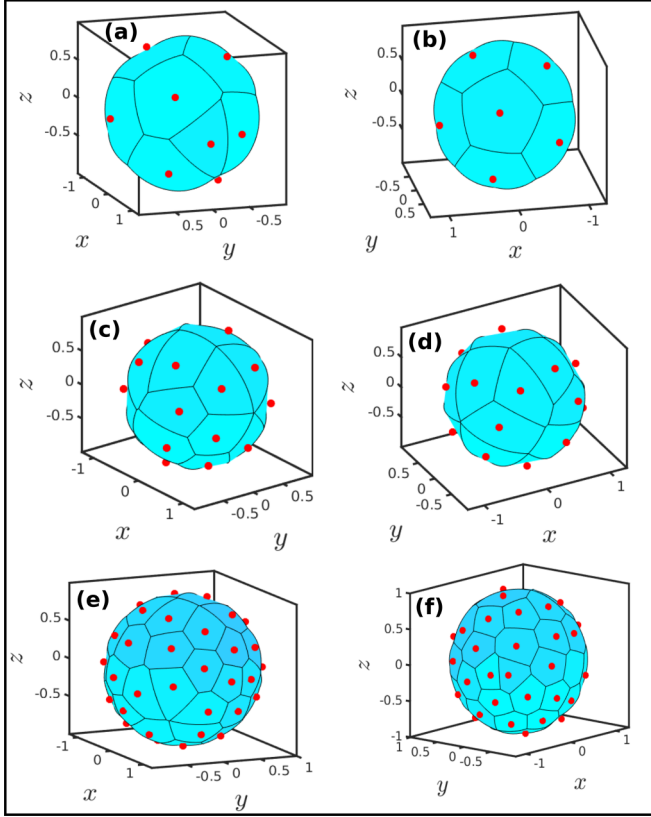


FIG. 13. Voronoi diagram with two different orientations for electrons in the First shell [shown in subplots (a), (b)], second shell [shown in subplots (c), (d)] and in the third shell [shown in subplots (e), (f)] having 12, 20, and 50 electrons, respectively.

Fig. 14 we show the number of electrons (N) which have been collected as a function of the time of their arrival in units of ω_{pe} . It is clear from the figure that it takes 100 s of plasma period for the electrons to arrive and shield the charge almost completely. While initially, the accumulation is relatively fast, it slows down considerably at the later stage. There is no change after about $t\omega_{pe} = 100$ when about 96 electrons have accumulated in the shielding cloud.

C. Comparison with Debye shielding

We now study the 3D radial potential profile obtained numerically after the shielding process has taken place and compare it with the Debye shielding profile. Such a comparison has been shown in Fig. 15. The blue line shows the theoretical Debye shielding profile, whereas the red dotted line is the potential profile that has been obtained from the simulation. Here too like 2D, we observe that the numerically obtained potential profile differs from the theoretical Debye

TABLE I. Number of polygons

Shell	Octagon	Heptagon	Hexagons	Pentagons	Tetragons
First	0	0	1	9	0
Second	0	2	6	8	1
Third	1	4	27	17	0

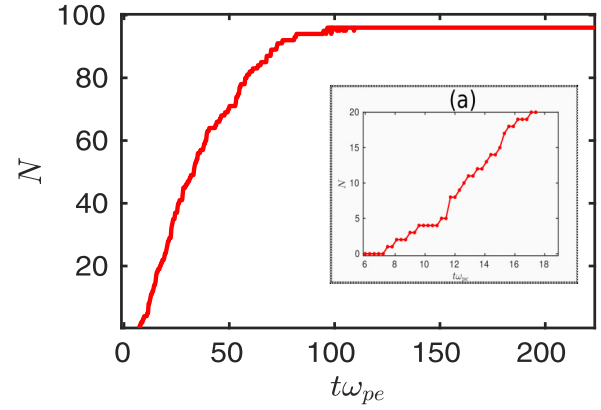


FIG. 14. Plot of number of electrons (N), near the external perturbation, with normalized time. Subplot (a) corresponds to the zoomed plot at initial time.

profile. In fact, due to the discrete arrangement of the electrons in various spherical shells, a sudden fall is also noticed in the profile. The zoomed-inset shows this more clearly in the figure. The location of this fall does not seem to be of statistical nature and occurs at the same location for the chosen set of parameters in a particular simulation confirming the uniqueness of the 3D pattern that forms.

We have also simulated the 2D and 3D ultracold electron-ion plasma with different values of LJ parameters, i.e., epsilon (ϵ) and sigma (σ). We observed that even when ϵ and σ are changed the shielding electrons still accumulate along various spherical shells. However, the location of the sharp dip in the potential profile does change when the value of σ in the Lenard-Jones potential is varied. When we increase the value of parameter σ to such an extent that it is greater than the Debye length (λ_D) the shielding of the potential becomes broader. This has been illustrated in Fig. 16.

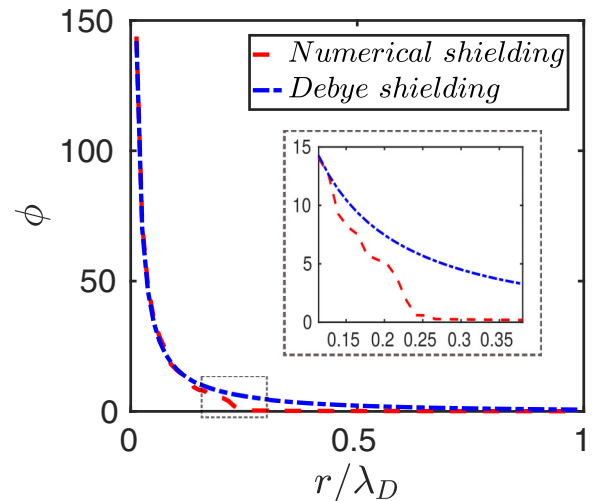


FIG. 15. Plot of potential profile as a function of normalized distance from external perturbation having charge $100Q_i$ and value of LJ parameter (σ) is 8.64×10^{-9} , i.e., smaller than the Debye length (λ_D) 7.88×10^{-8} . Here, the blue and red curve corresponds to the potential in normal electron-ion plasma and ultracold plasma, respectively, and subplot (a) represents the zoomed plot of the rectangular region shown by dotted lines.

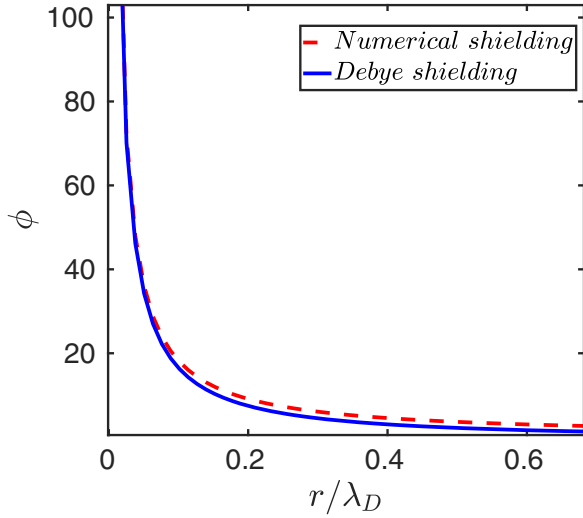


FIG. 16. Plot of potential profile as a function of normalized distance from external perturbation. Here, the value of LJ parameter (σ) is 8.64×10^{-8} , i.e., larger than the Debye length (λ_D). The blue and red curve corresponds to potential in normal electron-ion plasma and ultracold plasma, respectively.

VI. 3D BOUND STRUCTURES

In the simulations that we have carried out so far, we have observed only 2D bound-state formation. The bound state shows considerable stability and survives for a long time in the plasma where it faces constant bombardments from other particles. In this section, we explore the stability of a couple of chosen bound structures in isolation by tracking their evolution.

We first study the stability of the ring structure shown in Fig. 17(a) as an initial configuration and track its evolution. It quickly (within a fraction of the plasma period) attains the form shown in Fig. 17(b). We also placed a pair of rings on top of each other [Fig. 17(c)] and a linked pair of rings [Fig. 17(e)]. Both these configurations relax immediately to a cuboid form as shown in Figs. 17(d) and 17(f). It appears as a puzzle that the ring structure, which was stable in the presence of background plasma and survived for several plasma periods, is unstable and quickly relaxes to the cuboid structure in the absence of background plasma. It should also be noted that the final configuration is a 3D bound state which was never observed in the plasma.

We now look at the energetics of the ringed and the cuboid structure. The interparticle spacings of the two-ringed and the cuboid structure are shown in Fig. 18. The total potential energy of the ringed structure and the cuboid structure in terms of the interparticle spacings shown in Fig. 18 has been evaluated.

$$PE_{pc}^{ring} = 6 \frac{Q_i Q_j}{4\pi\epsilon_0} \left(\frac{-3}{a} + \frac{2}{b} - \frac{1}{c} + \frac{2}{d} - \frac{2}{e} + \frac{1}{f} \right), \quad (5)$$

$$PE_{ij}^{ring} = 6[2V_{ij}(a) + 2V_{ij}(b) + V_{ij}(c) + 2V_{ij}(d) + V_{ij}(e) + V_{ij}(f)], \quad (6)$$

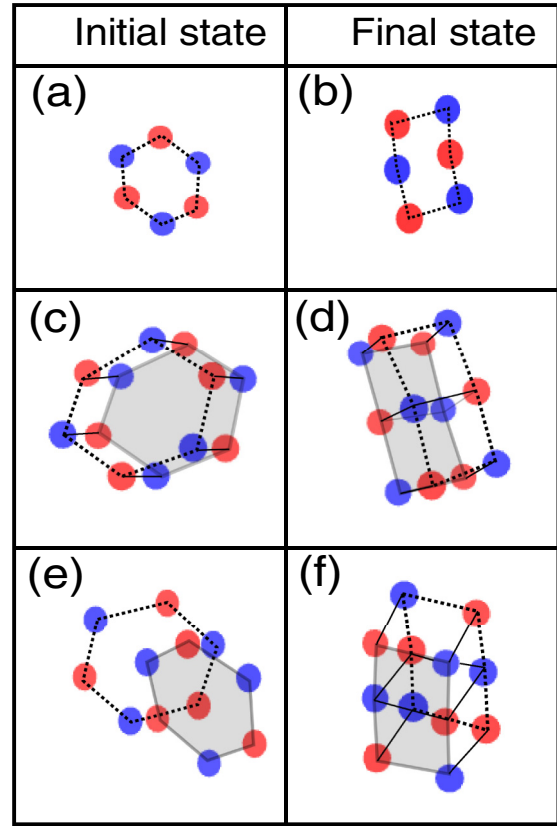


FIG. 17. Schematic representation of initial and final states of bound structures in 3D (without background plasma). Here, red and blue dots correspond to electrons and ions and subplots (a), (c), (e) represents the initial states whereas, subplots (b), (d), (f) show the final states.

whereas all the parameters in terms of a are

$$b = 2a \sin(60^\circ), \quad c = 2a, \\ d = \sqrt{2}a, \quad e = 2a, \quad f = \sqrt{5}a.$$

The total potential energy of ringed structure is

$$PE^{ring}(a) = PE_{pc}^{ring} + PE_{ij}^{ring},$$

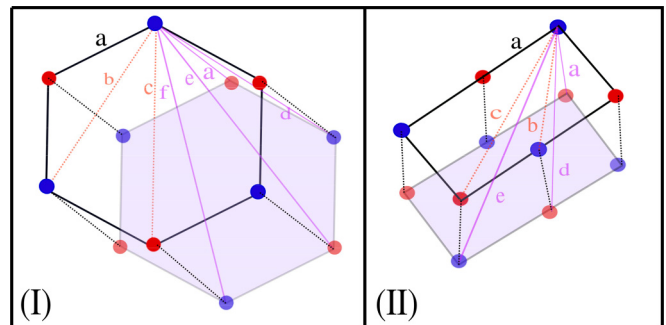


FIG. 18. Schematic representation of the ringed and cuboid structure.

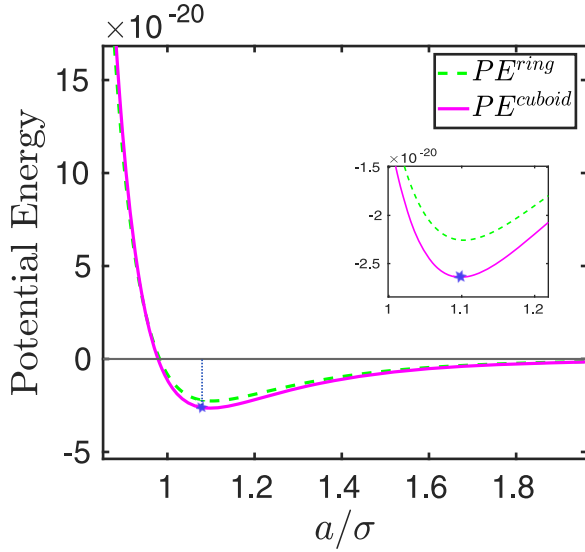


FIG. 19. Plot of the total potential energy of ringed (green) and cuboid structure (magenta) as a function of interparticle spacing which is normalized with the LJ parameter σ . Here, the star represents the minima in the potential energy and zoomed view of minima is shown in inset.

whereas

$$PE_{\text{pC}}^{\text{cuboid}} = \frac{Q_i Q_j}{4\pi\epsilon_0} \left(\frac{-18}{a} + \frac{22}{b} - \frac{8}{c} - \frac{8}{d} + \frac{4}{e} \right), \quad (7)$$

$$PE_{\text{lj}}^{\text{cuboid}} = 20V_{\text{lj}}(a) + 4V_{\text{lj}}(2a) + 22V_{\text{lj}}(b) + 8V_{\text{lj}}(c) + 8V_{\text{lj}}(d) + 4V_{\text{lj}}(e), \quad (8)$$

whereas all the parameters in terms of a are

$$b = \sqrt{2}a, \quad c = \sqrt{5}a, \\ d = \sqrt{6}a, \quad e = \sqrt{3}a.$$

The total potential energy for cuboid structure is

$$PE^{\text{cuboid}}(a) = PE_{\text{pC}}^{\text{cuboid}} + PE_{\text{lj}}^{\text{cuboid}}.$$

We have then plotted the expression for the potential energy for the two cases as a function of a/σ as shown in Fig. 19. The green and magenta curve corresponds to ringed and cuboid structures, respectively. The potential energy of the cuboid structure is found to be less than the overlapped ring structure. We believe this is the reason for favoring their formation in isolation. The presence of plasma clearly seems to modify this. It is also observed that at large values of interparticle distance the potential energy approaches zero, whereas, for shorter distances, it has high values. But at a certain separation, the potential energy is negative and has a minimum value. At this separation, the bound clusters are formed. Thus, the minima in the potential plot can in fact be viewed as the bound state energy of the cluster. Thus, the height of the blue dashed line shown in Fig. 19 represents the bound state energy of the cluster.

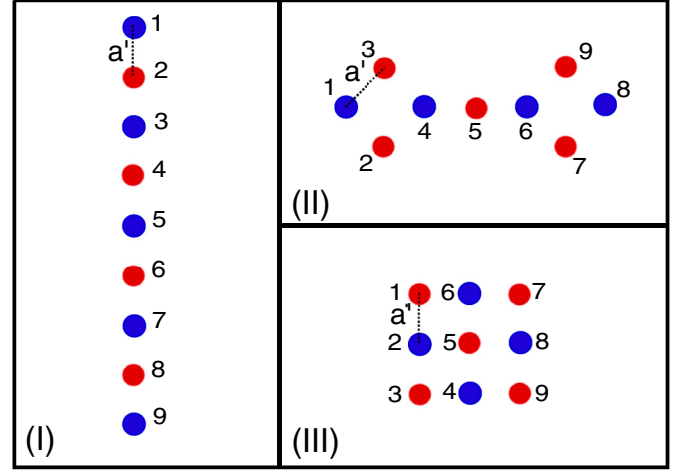


FIG. 20. Schematic representation of bound structures of subplot (b), (e), (g) of Fig. 1.

VII. SUMMARY

We have simulated an ultracold collection of an equal number of negative and positively charged particles (e.g., like electrons and ions, albeit their mass ratio is chosen to be different from the realistic case for ease of computation) in 2D and 3D by MD simulation in which both species are strongly coupled. The collapse between the unlike charge particles has been avoided by choosing repulsive interaction at short distances between these particles. Here we have chosen the particles to be interacting with a short-range LJ pair potential, whereas at large distances their interaction is governed by the Coulomb potential. At equilibrium, we have observed many types of bound structure formation. With the introduction of external perturbation (highly charged and massive point particle) we observe the expected phenomena of shielding. The particles are in a strongly coupled regime, therefore, the shielding cloud arranges in specific patterns. The shielding potential profile unlike the weakly coupled cases is determined by the choice of the LJ parameter of σ defining the distance at which the interparticle potential is minimum. In the crystalline pattern, the interparticle distance gets determined by this parameter. Thus, when σ is larger than the Debye length, the shielding is broader than expected from the Debye screening process. However, when it is smaller than the Debye length the screening is sharper. Thus, one needs to be cautious while drawing inferences of certain plasma properties while simulating the ultracold strongly coupled plasma using the short-range repulsive form to overcome the blowing up of the attractive potential amidst oppositely charged particles.

In literature, a lot of other forms of potential have been chosen to overcome the problem of the short-range Coulomb attraction [37,45,46]. For instance, the choice of the potential of the form $\frac{-e^2}{r} \{1 - \exp(\frac{-r^2}{(\alpha a)^2})\}$ in Ref. [37] also rescues the collapse from the Coulomb interaction. Here the parameter αa can be adjusted to appropriately define the repulsive core. For both LJ and this form of potential the minima in the potential profile occurs at a finite value of r . We observe that this aids the formation of clusters where atoms get arranged at distances defined by the location of the minimum in

potential. We, however, wish to point out that in the context of dense plasmas, the interaction potential has often been chosen as $\frac{-e^2}{r}\{1 - \exp^{-Cr}\}$ [45,46], where C defines as the inverse De-Broglie wavelength. Our investigations for this interaction potential do not yield any structure formation. This can be understood by realizing that for this case the minimum of the potential does not occur at a finite value of interparticle separation r .

ACKNOWLEDGMENTS

This research work has been supported by the Core Research Grant (Grant No. CRG/2018/000624) of the Department of Science and Technology, Ministry of Science and Technology, India. We also acknowledge support from the J.C. Bose Fellowship grant (Grant No. JCB-000055/2017) from the Science and Engineering Board (SERB), Govt. of

India. The authors thank IIT Delhi HPC facility for computational resources. M.Y. is thankful to the University Grants Commission (Grant No. 1316/CSIR-UGC NET DEC.2017) for funding the research. The authors also thank the Aman Singh Katariya for helpful discussion and the anonymous referee, whose comments have led to significant improvement of the manuscript.

APPENDIX: POTENTIAL ENERGIES FOR BOUND STRUCTURES

The potential energies for the three configurations in Figs. 1(b), 1(e), and 1(g) are calculated analytically in terms of a' . Here a' is the separation between the nearest-neighbor particles in these configurations and is found to be the same for all configurations. The potential energy for linear chain structure [Fig. 20(I)] is

$$PE_{\text{PC}}^{\text{I}} = \frac{Q_i Q_j}{4\pi\epsilon_0} \left(\frac{-8}{a'} + \frac{7}{2a'} - \frac{6}{3a'} + \frac{5}{4a'} - \frac{4}{5a'} + \frac{3}{6a'} - \frac{2}{7a'} + \frac{1}{8a'} \right), \quad (\text{A1})$$

$$PE_{\text{ij}}^{\text{I}} = 8V_{\text{ij}}(a') + 7V_{\text{ij}}(2a') + 6V_{\text{ij}}(3a') + 5V_{\text{ij}}(4a') + 4V_{\text{ij}}(5a') + 3V_{\text{ij}}(6a') + 2V_{\text{ij}}(7a') + V_{\text{ij}}(8a'). \quad (\text{A2})$$

The total potential energy of linear chain structure is

$$PE^{\text{I}}(a') = PE_{\text{PC}}^{\text{I}} + PE_{\text{ij}}^{\text{I}}.$$

After using the value of a' , the total potential energy of linear chain structure is -0.47×10^{-21} J, whereas

$$PE_{\text{PC}}^{\text{II}} = \frac{Q_i Q_j}{4\pi\epsilon_0} \left(\frac{-10}{r_{12}} + \frac{1}{r_{46}} + \frac{4}{r_{14}} - \frac{2}{r_{15}} + \frac{4}{r_{16}} - \frac{4}{r_{17}} + \frac{1}{r_{18}} + \frac{4}{r_{25}} - \frac{4}{r_{26}} + \frac{2}{r_{29}} \right), \quad (\text{A3})$$

$$PE_{\text{ij}}^{\text{II}} = 10V_{\text{ij}}(r_{12}) + V_{\text{ij}}(r_{46}) + 4V_{\text{ij}}(r_{14}) + 2V_{\text{ij}}(r_{15}) + 4V_{\text{ij}}(r_{16}) + 4V_{\text{ij}}(r_{17}) + V_{\text{ij}}(r_{18}) + 4V_{\text{ij}}(r_{25}) + 4V_{\text{ij}}(r_{26}) + 2V_{\text{ij}}(r_{29}), \quad (\text{A4})$$

where, r_{ij} is the distance between i th and j th particle, whereas all the parameters in terms of a' are

$$r_{12} = a', \quad r_{46} = 2a', \quad r_{14} = \sqrt{2}a', \quad r_{15} = (1 + \sqrt{2})a', \quad r_{16} = (2 + \sqrt{2})a', \quad r_{17} = (\sqrt{9 + 6\sqrt{2}})a', \\ r_{18} = (2 + 2\sqrt{2})a', \quad r_{25} = (\sqrt{2 + \sqrt{2}})a', \quad r_{26} = (\sqrt{5 + 2\sqrt{2}})a', \quad r_{29} = (\sqrt{8 + 4\sqrt{2}})a'.$$

The total potential energy for dumbbell structure [subplot (II) of Fig. 20] is

$$PE^{\text{II}}(a') = PE_{\text{PC}}^{\text{II}} + PE_{\text{ij}}^{\text{II}}.$$

After using the value of a' , the total potential energy of dumbbell structure is -2.29×10^{-21} J, whereas

$$PE_{\text{PC}}^{\text{III}} = \frac{Q_i Q_j}{4\pi\epsilon_0} \left(\frac{-12}{r_{12}} + \frac{8}{r_{15}} + \frac{2}{r_{19}} - \frac{8}{r_{18}} + \frac{6}{r_{17}} \right), \quad (\text{A5})$$

$$PE_{\text{ij}}^{\text{III}} = 12V_{\text{ij}}(r_{12}) + 8V_{\text{ij}}(r_{15}) + 2V_{\text{ij}}(r_{19}) + 8V_{\text{ij}}(r_{18}) + 6V_{\text{ij}}(r_{17}), \quad (\text{A6})$$

whereas all the parameters in terms of a' are

$$r_{15} = \sqrt{2}a', \quad r_{19} = 2\sqrt{2}a', \quad r_{18} = \sqrt{5}a', \quad r_{17} = 2a'$$

The total potential energy for the square structure [subplot (III) of Fig. 20] is

$$PE^{\text{III}}(a') = PE_{\text{PC}}^{\text{III}} + PE_{\text{ij}}^{\text{III}}.$$

After using the value of a' , the total potential energy of a square structure is -4.13×10^{-21} J. It is thus clear that a square lattice has the maximum binding energy and hence is the most stable structure. However, a linear chain has the least binding energy, whereas the dumbbell structure has an intermediate binding energy.

- [1] V. N. Tsytovich, *Phys. Usp.* **50**, 409 (2007).
- [2] A. Filippov, A. Pal, and A. Starostin, *J. Exp. Theor. Phys.* **121**, 909 (2015).
- [3] S. Ratynskaia, U. De Angelis, S. Khrapak, B. Klumov, and G. Morfill, *Phys. Plasmas* **13**, 104508 (2006).
- [4] A. Naji, S. Jungblut, A. G. Moreira, and R. R. Netz, *Physica A* **352**, 131 (2005).
- [5] C. Holm, P. Kékicheff, and R. Podgornik, *Electrostatic Effects in Soft Matter and Biophysics*, Vol. 46 (Springer Science & Business Media, Berlin, 2001).
- [6] Y. Levin, *Rep. Prog. Phys.* **65**, 1577 (2002).
- [7] M. Z. Bazant, K. Thornton, and A. Ajdari, *Phys. Rev. E* **70**, 021506 (2004).
- [8] M. S. Kilic, M. Z. Bazant, and A. Ajdari, *Phys. Rev. E* **75**, 021503 (2007).
- [9] V. Fortov, I. Iakubov, and A. Khrapak, *Physics of Strongly Coupled Plasma*, Vol. 135 (Oxford University Press, Oxford, UK, 2006).
- [10] S. Ichimaru, *Rev. Mod. Phys.* **54**, 1017 (1982).
- [11] J. H. Chu and Lin I, *Phys. Rev. Lett.* **72**, 4009 (1994).
- [12] H. Thomas, G. E. Morfill, V. Demmel, J. Goree, B. Feuerbacher, and D. Möhlmann, *Phys. Rev. Lett.* **73**, 652 (1994).
- [13] P. Kaw and A. Sen, *Phys. Plasmas* **5**, 3552 (1998).
- [14] M. S. Murillo, *Phys. Plasmas* **11**, 2964 (2004).
- [15] S. Kumar, S. K. Tiwari, and A. Das, *Phys. Plasmas* **24**, 033711 (2017).
- [16] A. Das, V. Dharodi, and S. Tiwari, *J. Plasma Phys.* **80**, 855 (2014).
- [17] S. K. Tiwari, A. Das, A. Sen, and P. Kaw, *Phys. Plasmas* **22**, 033706 (2015).
- [18] A. Kumar, A. Das, and P. Kaw, *Phys. Plasmas* **26**, 083702 (2019).
- [19] S. Kumar, B. Patel, and A. Das, *Phys. Plasmas* **25**, 043701 (2018).
- [20] A. Das, S. K. Tiwari, P. Kaw, and A. Sen, *Phys. Plasmas* **21**, 083701 (2014).
- [21] S. K. Tiwari, A. Das, D. Angom, B. G. Patel, and P. Kaw, *Phys. Plasmas* **19**, 073703 (2012).
- [22] A. Das and P. Kaw, *Phys. Plasmas* **21**, 062102 (2014).
- [23] V. S. Dharodi, B. Patel, and A. Das, *J. Plasma Phys.* **88**, 905880103 (2022).
- [24] B. Veerasha, A. Das, and A. Sen, *Phys. Plasmas* **12**, 044506 (2005).
- [25] S. Maity and A. Das, *Phys. Plasmas* **26**, 023703 (2019).
- [26] S. Maity and G. Arora, *Sci. Rep.* **12**, 1 (2022).
- [27] S. Maity, A. Das, S. Kumar, and S. K. Tiwari, *Phys. Plasmas* **25**, 043705 (2018).
- [28] P. Deshwal, M. Yadav, C. Prasad, S. Sridev, Y. Ahuja, S. Maity, and A. Das, *Chaos* **32**, 063136 (2022).
- [29] S. Maity, P. Deshwal, M. Yadav, and A. Das, *Phys. Rev. E* **102**, 023213 (2020).
- [30] H. Van Horn, *Science* **252**, 384 (1991).
- [31] T. C. Killian, S. Kulin, S. D. Bergeson, L. A. Orozco, C. Orzel, and S. L. Rolston, *Phys. Rev. Lett.* **83**, 4776 (1999).
- [32] S. Kulin, T. C. Killian, S. D. Bergeson, and S. L. Rolston, *Phys. Rev. Lett.* **85**, 318 (2000).
- [33] T. C. Killian, M. J. Lim, S. Kulin, R. Dumke, S. D. Bergeson, and S. L. Rolston, *Phys. Rev. Lett.* **86**, 3759 (2001).
- [34] E. A. Cummings, J. E. Daily, D. S. Durfee, and S. D. Bergeson, *Phys. Rev. Lett.* **95**, 235001 (2005).
- [35] L. Guo, R. H. Lu, and S. S. Han, *Phys. Rev. E* **81**, 046406 (2010).
- [36] S. G. Kuzmin and T. M. O'Neil, *Phys. Plasmas* **9**, 3743 (2002).
- [37] S. K. Tiwari, N. R. Shaffer, and S. D. Baalrud, *Phys. Rev. E* **95**, 043204 (2017).
- [38] S. L. Gilbert, J. J. Bollinger, and D. J. Wineland, *Phys. Rev. Lett.* **60**, 2022 (1988).
- [39] T. Pohl, T. Pattard, and J. M. Rost, *Phys. Rev. Lett.* **92**, 155003 (2004).
- [40] S. Plimpton, *J. Comput. Phys.* **117**, 1 (1995).
- [41] M. Heath, *Proceedings of the 8th SIAM Conference on Parallel Processing for Scientific Computing* (SIAM, Philadelphia, PA, 1997).
- [42] S. Nosé, *J. Chem. Phys.* **81**, 511 (1984).
- [43] W. G. Hoover, *Phys. Rev. A* **31**, 1695 (1985).
- [44] See Supplemental Material at <http://link.aps.org/supplemental/10.1103/PhysRevE.107.055214> for transition from linear-chain-bound structure to square-box-bound structure, for formation of bound structure having three electrons and three ions, and for evolution of crystalline structure around external perturbation.
- [45] C. Deutsch, *Phys. Lett. A* **60**, 317 (1977).
- [46] J.-P. Hansen and R. Mazighi, *Phys. Rev. A* **18**, 1282 (1978).